

Many-body quantum thermal machines in a Lieb-kagome Hubbard model

Saikat Sur,¹ Pritam Chattopadhyay,¹ Madhuparna Karmakar,^{2,*} and Avijit Misra^{3,†}

¹*Department of Chemical and Biological Physics & AMOS,
Weizmann Institute of Science, Rehovot 7610001, Israel*

²*Department of Physics and Nanotechnology, College of Engineering and Technology,
SRM Institute of Science and Technology, Kattankulathur, Chennai-603203, India*

³*Centre for Quantum Engineering, Research and Education (CQuERE),
TCG CREST, Salt Lake, Sector 5, Kolkata 700091, India*

(Dated: May 1, 2024)

Quantum many-body systems serve as a suitable working medium for realizing quantum thermal machines (QTM) by offering distinct advantages such as cooperative many-body effects, and performance boost at the quantum critical points. However, the bulk of the existing literature exploring the criticality of many-body systems in the context of QTMs involves models sans the electronic interactions, which are non-trivial to deal with and require sophisticated numerical techniques. Here we adopt the prototypical Hubbard model in two dimensions (2D) in the framework of the line graph Lieb-kagome lattice for the working medium of a multi-functional QTM. We resort to a non-perturbative, static path approximated (SPA) Monte Carlo technique to deal with the repulsive Hubbard model. We observe that in a Stirling cycle, in both the interacting and non-interacting limits, the heat engine function dominates and its performance gets better when the strain is induced from the kagome to the Lieb limit, while for the reverse the refrigeration action is preferred. Further, we show that the QTM performs better when the difference between the temperatures of the two baths is lower and the QTM reaches the Carnot limit in this regime. Further, we extensively study the performance of the QTM in the repulsive Hubbard interacting regime where the magnetic orders come into the picture. We explore the performance of the QTM along the quantum critical points and in the large interaction limit.

I. INTRODUCTION

With recent advancements towards miniaturized devices at the nanoscale, there has been an upsurge of activities in modeling and designing quantum thermal devices including quantum heat engines^{1–17}, refrigerators^{18–22}, diodes and transistors^{23–26}, transformers²⁷. Though the theoretical explorations have been much ahead, there have been successful experimental demonstrations of quantum heat engines (QHE) in trapped ions^{28–30}, nuclear magnetic resonance³¹, and nitrogen-vacancy centers in diamonds³² based setups. One of the main motivations of these explorations is to harness quantumness for better functioning of the QHE which includes exploiting non-thermal and squeezed baths^{33–36}, presence of quantum coherence in the working medium (WM)^{37,38}, quantum measurements^{39–42}.

Primarily the study of QHE has dealt with a single particle or a few⁴³. Considering many-body (MB) quantum systems as WM of a QHE is relatively new. Quantum MB systems have been employed to harness MB quantum correlation⁴⁴, quantum criticality^{45–47}, MB localization⁴⁸, super-radiance⁴⁹, minimizing friction^{50–53}, and investigate the effect of quantum statistics⁵⁴ in QHE. Quantum criticality has been proven to be a useful resource in MB-QHE^{47,55}.

The bulk of the existing literature exploring the criticality of MB in the context of QHE involves models sans the electronic interactions, which are non-trivial to deal with and require sophisticated numerical techniques. At the same time, electronic interactions in conjunction with competing correlations and/or geometric frustration of lattices are known to bring forth rich quantum phases and phase transitions^{56–63}. The aim of this work is to analyze such an interplay between quantum correlations and geometric frustration in the light of quantum thermodynamics, thereby proposing its prospective application

as a quantum thermal machine (QTM).

Our starting Hamiltonian corresponds to the prototypical Hubbard model in two dimensions (2D) in the framework of the line graph Lieb-kagome lattice^{64,65}. The unprecedented control over the engineering and subsequent tuning of these lattices in ultracold atomic gases^{66,67}, optically induced photonic systems^{68–70}, artificial lattices engineered through lithography and atomic manipulations^{71–73} and more recently in a metal-organic framework (MOF)⁷⁴ have provided the required impetus to the search for their potential applications. In the non-interacting limit, this lattice with a three-site unit cell hosts three electronic dispersion bands as two dispersive and one flat band. The position of the electronic bands and the corresponding underlying Brillouin zone provides the Lieb and the kagome lattices with their distinct properties that have been investigated extensively. The impact of the inclusion of electronic interactions in this system shows up as two important observations viz. (*i*) beyond a critical interaction, magnetic correlation sets in, demarcating the low-temperature phases to be magnetically disordered and ordered, (*ii*) the electronic transport, controlled by the underlying band structure quantifies the different interaction regimes of the system as metallic and insulating⁷⁵. Being a line-graph lattice the band structure between the Lieb and kagome limits can be smoothly evolved by suitable strain engineering, thereby tuning the thermodynamic, spectroscopic, and transport properties of this system.

In the next few sections, we discuss the impact of this strain engineering on electronic dispersion and explore its implications on the function of a QTM. Our primary inference from this work is that by suitable strain engineering one can achieve four working domains such as quantum heat engine (QHE), quantum refrigerator (QR), quantum accelerator (QA), and quantum heater (QH) by running a Stirling cycle^{76–80}. The

QHE domain is more feasible and its performance gets better when we engineer the strain from the kagome limit to the Lieb limit in the line graph lattice. Conversely, for QR, it is better, if the strain is engineered in the reverse direction. The performance of both QHE and QR gets better when the temperature difference between the two operating baths, hot and cold namely, is lower and the Carnot limit is achieved in this region. This is valid for both the interacting and the non-interacting cases.

For the interacting case, though a low-temperature difference between the working bath is preferred, unlike the non-interacting case the favorable working temperatures are not close to the zero temperature. Interestingly, at the critical point where the system exhibits a magnetic transition from a paramagnetic metal to an anti-ferromagnetic metal, the QTM performs well through the entire parameter space of the bath temperature, close to zero being the most favorable region.

The article is organized as follows. In Sec. II, we analyze the model of the WM, a 2D line graph lattice (Lieb and kagome) having onsite repulsive Hubbard interaction. Then we discuss the Stirling cycle and thermodynamic quantifiers of heat and work and performance bounds of the same in Sec. III. In Sec. IV, we discuss the results for both the non-interacting (Sec. IV A) and interacting (Sec. IV B) cases. Finally, we conclude in Sec. V.

II. MODEL

The prototypical repulsive Hubbard Hamiltonian on a 2D line graph Lieb-kagome lattice reads as

$$H = \mu \sum_{i,\sigma} c_{i,\sigma}^\dagger c_{i,\sigma} + \sum_{\langle ij \rangle, \sigma} t_{ij} c_{i,\sigma}^\dagger c_{j,\sigma} + \sum_{\langle\langle ij \rangle\rangle, \sigma} t'_{ij} c_{i,\sigma}^\dagger c_{j,\sigma} + \text{H.c.} + U \sum_i \hat{n}_{i\uparrow} \hat{n}_{i\downarrow}. \quad (1)$$

where, t_{ij} corresponds to the nearest neighbor hopping and $t_{ij} = t = 1$ sets the reference energy scale of the model. The applied strain is quantified in terms of $t'_{ij} = t'$. $U > 0$ corresponds to the repulsive Hubbard interaction. We work at the half-filling and the chemical potential μ is adjusted to achieve the same. The strain-induced excursion of the lattice and therefore the corresponding electronic band structure between the Lieb and the kagome limits is represented in Fig. 1.

In the presence of interactions ($U \neq 0$), the model is made numerically tractable via Hubbard-Stratonovich (HS) decomposition of the four-fermion term^{81,82}, introducing a vector $\mathbf{m}_i(\tau)$ and a scalar $\phi_i(\tau)$ (bosonic) auxiliary fields at each site, which couples to the spin and the charge channels, respectively. The problem is addressed via the static path approximated (SPA) Monte Carlo technique wherein the model is envisaged as an effective spin-fermion model with the random, fluctuating, "classical" background of the auxiliary fields coupled to the free fermions. The ϕ_i field is treated at the saddle point level as $\phi_i \rightarrow \langle \phi_i \rangle = \langle n_i \rangle U/2$ (where, $\langle n_i \rangle$ is the number density of the fermions), while the complete spatial fluctuations of \mathbf{m}_i are retained. The quantum thermodynamic properties

are analyzed based on the proper identification of heat and work in the quantum domain^{83,84}. Thereby, we analyze the performance of a multifunctional (see Table. I) QTM. The results presented in this paper correspond to a system size of $3 \times L^2$, with $L = 16$, and are verified to be robust against finite system size effects. The details of the numerical technique are presented in the appendix.

We begin the analysis of our results with the non-interacting limit by setting $U = 0$ in Eq. (1). To evaluate the energy spectrum, we transform the Hamiltonian in the momentum space as $\mathcal{H} = \sum_{\mathbf{k}} \Phi_{\mathbf{k}}^\dagger H_{\mathbf{k}} \Phi_{\mathbf{k}}$ with $\Phi_{\mathbf{k}}^\dagger = (c_{\mathbf{A}\mathbf{k}}^\dagger \ c_{\mathbf{B}\mathbf{k}}^\dagger \ c_{\mathbf{C}\mathbf{k}}^\dagger)$, where

$$H_{\mathbf{k}} = \begin{pmatrix} 0 & A_{\mathbf{k}} & B_{\mathbf{k}} \\ A_{\mathbf{k}} & 0 & C_{\mathbf{k}} \\ B_{\mathbf{k}} & C_{\mathbf{k}} & 0 \end{pmatrix}. \quad (2)$$

Here $A_{\mathbf{k}} = -2 \cos \frac{k_x}{2}$, $B_{\mathbf{k}} = -2 \cos \left(-\frac{k_x}{2} \cos \theta + \frac{k_y}{2} \sin \theta \right)$, and $C_{\mathbf{k}} = -t_{AC}^1 \cos \left(\frac{k_x}{2} (1 + \cos \theta) - \frac{k_y}{2} \sin \theta \right) - t_{AC}^2 \cos \left(\frac{k_x}{2} (1 - \cos \theta) + \frac{k_y}{2} \sin \theta \right)$. The strain is quantified in terms of the parameters t_{AC}^1 and t_{AC}^2 between the sites A and C as⁸⁵

$$t_{AC}^1 = \exp \left[\eta (1 - 2 \cos \frac{\theta}{2}) \right], \\ t_{AC}^2 = \exp \left[\eta (1 - 2 \sin \frac{\theta}{2}) \right], \quad (3)$$

where the parameter η governs the rate at which the strain diminishes with distance. A higher η results in a more gradual decrease in the band curvature, leading to a flatter band. Conversely, a smaller η is more adept at capturing the transition of the band structure from Lieb to kagome. For $\eta = 8$, we achieve relatively flat bands and smooth transitions between the two lattices⁸⁶. The angle θ is tuned within the range of $[\frac{\pi}{2}, \frac{2\pi}{3}]$. The lower and the upper bounds correspond to the Lieb and the kagome lattice, respectively. In the Lieb limit ($\theta = \pi/2$), with the strain being, $t_{AC}^1 = t_{AC}^2 = \exp[\eta(1 - \sqrt{2})]$. On the other hand, in the kagome limit ($\theta = 2\pi/3$), with the corresponding strain being parametrized as, $t_{AC}^1 = t = 1$ and $t_{AC}^2 = \exp[\eta(1 - \sqrt{3})]$. The transition between the Lieb and kagome lattices is observed at $\theta^* = 7\pi/12$.

Now diagonalizing $H_{\mathbf{k}}$, we get the three respective eigenvalues

$$\varepsilon_{\mathbf{k},j} = \sqrt{\frac{2}{3}} (A_{\mathbf{k}}^2 + B_{\mathbf{k}}^2 + C_{\mathbf{k}}^2)^{1/2} \times \\ \cos \left[\frac{1}{3} \cos^{-1} \left(\frac{3\sqrt{3}A_{\mathbf{k}}B_{\mathbf{k}}C_{\mathbf{k}}}{(A_{\mathbf{k}}^2 + B_{\mathbf{k}}^2 + C_{\mathbf{k}}^2)^{3/2}} \right) - \frac{2\pi(j-1)}{3} \right], \\ j = 1, 2, 3. \quad (4)$$

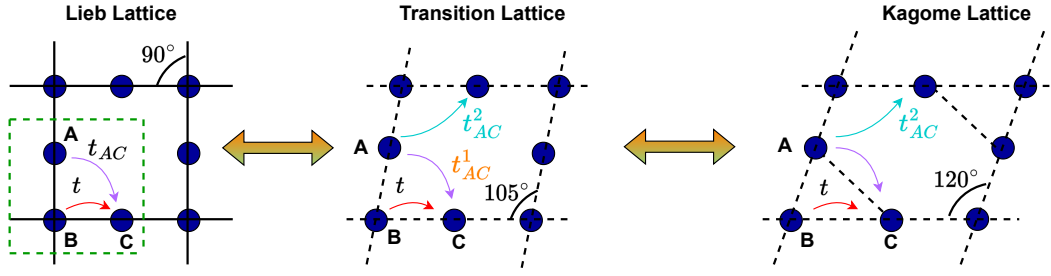


Figure 1. Schematic diagram showing the strain-induced evolution of the lattice structure between the Lieb and the kagome limits.

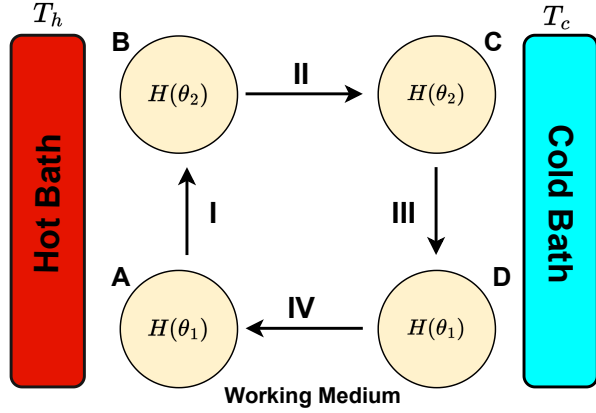


Figure 2. Schematic representation of the Stirling cycle. $A \rightarrow B$ and $C \rightarrow D$ are the two isothermal steps where the Hamiltonian parameter θ is changed when the WM is in contact with the heat baths at temperatures T_h and T_c respectively. $B \rightarrow C$ and $D \rightarrow A$ are the two isochoric thermalization steps in contact with the heat baths at temperatures T_h and T_c respectively, while the Hamiltonian parameter θ is fixed.

III. STIRLING CYCLE AND THERMODYNAMIC QUANTITIES

A quantum Stirling cycle^{76–80} consists of four steps (Fig. 2). First ($A \rightarrow B$), the WM is in equilibrium with the heat bath at temperature T_h , while the Hamiltonian parameter is isothermally changed, $\theta_1 \rightarrow \theta_2$ (Eq. (3)). In the second step ($B \rightarrow C$), the WM is detached from the hot bath and connected with a cold bath at a temperature T_c with which it thermalizes isochorically without performing any mechanical work. Next ($C \rightarrow D$), the WM is brought back to its initial Hamiltonian configuration isothermally ($\theta_2 \rightarrow \theta_1$) while keeping the system connected to the cold bath. In the final step ($D \rightarrow A$), the system is detached from the cold bath and connected to the hot bath where it undergoes an isochoric thermalization process without performing any mechanical work. Thus, the WM fully recovers to its initial state and the cycle is completed.

The total heat transferred to the system from the bath in the isothermal processes ($A \rightarrow B$) and ($C \rightarrow D$), while keeping the system in equilibrium with the bath at temperature T_h and T_c respectively, are combinations of the mechanical works performed due to deformation of the potential and the change

of the internal energies. Thus the heat transferred to the bath from the system during two isothermal processes is given by

$$Q_{AB} = -(U_{T_h}^{\theta_2} - U_{T_h}^{\theta_1} + k_B T_h \ln Z_{T_h}^{\theta_2} - k_B T_h \ln Z_{T_h}^{\theta_1}), \quad (5)$$

and

$$Q_{CD} = -(U_{T_c}^{\theta_1} - U_{T_c}^{\theta_2} + k_B T_c \ln Z_{T_c}^{\theta_1} - k_B T_c \ln Z_{T_c}^{\theta_2}), \quad (6)$$

respectively. Here, Z_T^θ is the partition function evaluated as

$$Z_T^\theta = \sum_{\mathbf{k}} \sum_j e^{-\frac{\epsilon_{\mathbf{k},j}^\theta}{T}} = \frac{1}{4\pi^2} \sum_j \int \int dk_x dk_y e^{-\frac{\epsilon_{\mathbf{k},j}^\theta}{T}} \quad (7)$$

and the internal energy U_T^θ is evaluated as $T^2 \frac{\partial}{\partial T} \ln Z_T^\theta$. On the other hand, the heat transferred to the system during the isochoric thermalization processes ($B \rightarrow C$) and ($D \rightarrow A$) are the differences between the average energies of the initial and the final configurations as no mechanical work has been considered. Therefore, we have

$$Q_{BC} = -(U_{T_c}^{\theta_2} - U_{T_c}^{\theta_1}), \quad \text{and} \quad Q_{DA} = -(U_{T_h}^{\theta_1} - U_{T_h}^{\theta_2}). \quad (8)$$

Provided all the processes involved in the cycle are reversible and no leakage takes place, the expressions for the net work done on the system W and the heat transferred to the system with the hot and cold baths, Q_h and Q_c after completion of one cycle are given as follow:

$$\begin{aligned} W &= (Q_{AB} + Q_{BC} + Q_{CD} + Q_{DA}) \\ &= -T_h \ln \frac{Z_{T_h}^{\theta_2}}{Z_{T_h}^{\theta_1}} + T_c \ln \frac{Z_{T_c}^{\theta_2}}{Z_{T_c}^{\theta_1}}, \\ Q_h &= -(Q_{AB} + Q_{DA}) = T_h \ln \frac{Z_{T_h}^{\theta_2}}{Z_{T_h}^{\theta_1}} + U_{T_h}^{\theta_2} - U_{T_h}^{\theta_1}, \\ Q_c &= -(Q_{BC} + Q_{CD}) = -T_c \ln \frac{Z_{T_c}^{\theta_2}}{Z_{T_c}^{\theta_1}} - U_{T_h}^{\theta_2} + U_{T_c}^{\theta_1}. \end{aligned} \quad (9)$$

By the principle of conservation of energy or the first law of thermodynamics, one can check that $Q_h + Q_c + W = 0$. Importantly, it has been established that the maximal isothermal work extraction also in the quantum domain is given by

the change in free energy $\Delta F^{83,84}$, where

$$F = U - TS. \quad (10)$$

Here, S is the von Neuman entropy of the WM ρ as quantified by $S(\rho) = -\text{Tr}[\rho \log \rho]$ and T is the temperature of the heat bath. One can check that work W in Eq. (9) follows it. If the quantities Q_h or Q_c are positive, the heat is flowing into the system, similarly, if work W is positive, work is done on the system. In conformity with the second law of thermodynamics, only four modes of operation are possible. The four possible modes can be identified by the signs of W , Q_h , and Q_c , as depicted in Table I.

Modes of operation	Q_h	Q_c	W
Engine	> 0	< 0	< 0
Refrigerator	< 0	> 0	> 0
Accelerator	> 0	< 0	> 0
Heater	< 0	< 0	> 0

Table I. Different modes of operation of a quantum thermodynamic cycle.

The efficiency η of the engine is given by

$$\eta = \frac{|W|}{Q_h}, \quad (11)$$

and the coefficient of the performance (COP) of the refrigerator is given as

$$\eta_R = \frac{Q_c}{|W|}. \quad (12)$$

Given a pair of thermal baths, the maximum efficiency or coefficient of performance is obtained for the Carnot cycle, a theoretical proposition with only reversible cycles. We present the efficiency of the engine and coefficient of performance of the refrigerator scaled by the same as its Carnot counterpart in this article. The efficiency of a Carnot engine and the coefficient of performance of the Carnot refrigerator are given respectively as

$$\eta^{max} = 1 - \frac{T_c}{T_h}, \quad \text{and} \quad \eta_R^{max} = \frac{T_c}{T_h - T_c}. \quad (13)$$

IV. PERFORMANCE OF THE MANY-BODY QUANTUM THERMAL MACHINE

In this section, we investigate and analyze the thermodynamic performance of the many-body quantum thermal machine based on the Lieb-kagome Hubbard model. Interestingly, we observe that all four operational regimes are mentioned in the Table. I, i.e. QHE, QR, QA, and QH can be realized in our model by either tuning the strain, the bath temperatures, or the onsite repulsive Hubbard interaction. Thus, the model works as a multifunctional quantum thermal device. For

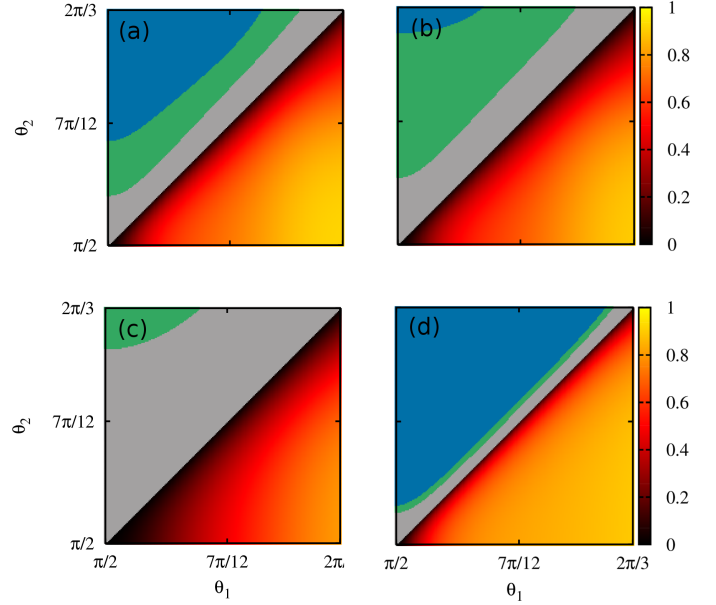


Figure 3. Demonstration of multi-functionality of the Stirling cycle by tuning the WM strain (θ_1, θ_2) without the onsite repulsive interaction, with different sets of bath temperatures: (a) $T_h = 0.02, T_c = 0.01$; (b) $T_h = 0.03, T_c = 0.01$; (c) $T_h = 0.2, T_c = 0.01$; (d) $T_h = 0.05, T_c = 0.04$. The refrigerator, the accelerator, and the heater regions are marked in blue, grey, and green respectively. The engine region is plotted with color density where the color denotes the engine efficiency.

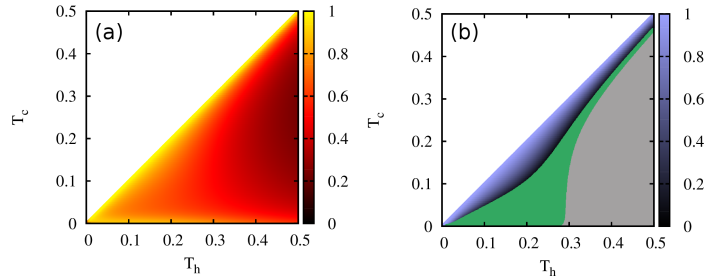


Figure 4. Function of the Stirling cycle with two fixed strain configurations (a) $\theta_1 = 2\pi/3, \theta_2 = \pi/2$; (b) $\theta_1 = \pi/2, \theta_2 = 2\pi/3$ as a function of the thermal bath temperatures. The refrigerator, the accelerator, and the heater regions are marked in blue, grey, and green respectively. The engine and refrigerator region is plotted with color density where the color denotes the efficiency and coefficient of performance (COP) of the engine and refrigerator respectively.

brevery, we present the analysis for the non-interacting ($U = 0$) and interacting ($U \neq 0$) WM in separate subsections.

A. For non-interacting working medium

We begin with the Stirling cycle by tuning the strain of the WM (θ_1, θ_2). The performance of the QHE and other func-

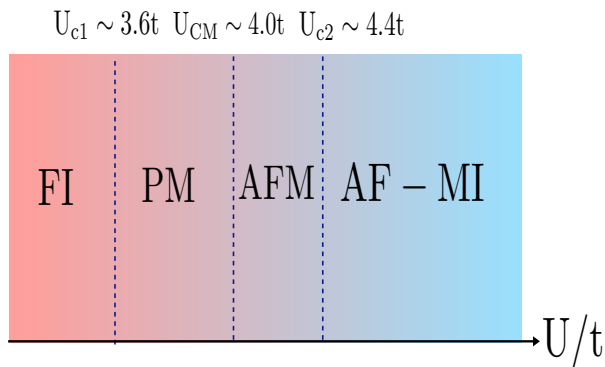


Figure 5. Low-temperature phase diagram (at $T = 0.01$) of the kagome Hubbard model at half filling mapping out the various thermodynamic phases as (i) Flat band Insulator (FI), (ii) Paramagnetic Metal (PM), (iii) Antiferromagnetic Metal (AFM) and (iv) Antiferromagnetic Mott Insulator (AF-MI)⁷⁵.

tional regions QR, QA, and QH have been shown in Fig. 3. It shows that we get the QHE performance better when we start the cycle from the Kagome limit and then move to the Lieb limit and the opposite for QR. The maximum efficiency of the QHE reaches the Carnot bound for the Lieb-kagome configuration, specifically when $\theta_1 = 2\pi/3$ and $\theta_2 = \pi/2$. In the low-temperature limit, the performance of the QHE and feasible region (in the strain parameter space) for it and QR increases when the difference between the two bath temperatures is lower. Moreover, we observe distinct signatures of all the functions of the proposed QTM. However, as the temperature difference increases, the characteristic features of the QR and QH diminish.

We further look into the role of temperature difference in Fig. 4 to substantiate our observation. It clearly shows that the efficiency or the coefficient of performance (COP) of the QHE or QR are higher near the $T_h = T_c$ line and for the configuration with $T_c \rightarrow 0$, $T_h \rightarrow \epsilon$ (where ϵ is close to zero) with fixed strain configuration.

B. For interacting working medium

Let us now explore the interacting WM. The interacting domain hosts several critical points. In the kagome limit the ground state phase diagram hosts several quantum critical points, as shown in Fig. 5. Here, the QPT U_{CM} corresponds to a magnetic transition between a paramagnetic and an antiferromagnetic metal. U_{c1} shows an insulator-metal transition (IMT), while U_{c2} corresponds to a metal-Mott insulator transition (MIT). The phases and transitions are determined based on various thermodynamics, spectroscopic, and electrical/optical transport properties, viz. magnetic correlations, structure factor, single-particle density of states, optical and electrical conductivity, etc.

These phases and phase transitions can also be captured based on the quantum information perspective based on indicators such as entanglement entropy, mutual information, etc.

and such studies have been reported for a square lattice that has a relatively simple phase diagram⁸⁷⁻⁹¹. The several standard Green's function-based techniques are used to calculate the relevant quantities viz. determinant quantum Monte Carlo, dynamical mean field theory, static path approximated quantum Monte Carlo, etc.

We demonstrate the behavior of the Stirling cycle with different values of the Hubbard interaction parameter computed from numerical analysis in Fig 6 (a-j) (see App. B for details regarding the analysis). We have chosen some representative values of U to display the changing of QHE, QR, QA, and QH and their relationship with the quantum phases in the model. Although introducing the interaction in the model does not drastically change the behavior of the cycle for a given set of strain parameters (cf Fig. 4), it is observed that the regions corresponding to different modes do change non-trivially showing the signature of various phases of the system.

For a cycle with the strain parameters ($\theta_1 = 2\pi/3, \theta_2 = \pi/2$), the regions of QH, QR and QA (where $W > 0$) exist in the mode-diagrams for $U = 1.0, 3.6$ and $U = 4.6$ (see Fig 6 (a), (b) and (d)) but missing for $U = 4.6$ and 9.0 when the bath temperatures are low. On the other hand, for a cycle with the strain parameters ($\theta_1 = \pi/2, \theta_2 = 2\pi/3$), a small region of QHE appears in the mode diagram for $U = 1.0, 3.6$ and $U = 4.6$ when the bath temperatures are low (see Fig 6 (f), (g) and (i)). Otherwise, in these cases, most of the mode-diagram is still dominated by the QHE mode (where $W < 0$) and QH, QA, QR modes (where $W > 0$) for the set of strain parameters ($\theta_1 = 3\pi/2, \theta_2 = \pi/2$) and ($\theta_1 = \pi/2, \theta_2 = 2\pi/3$) respectively, as already shown for the noninteracting counterpart.

This non-triviality of the results with the interacting model emerges as an artifact of the non-monotonic change in the energy levels of the system in both strain configurations. In other words, the behavior of the cycle will be determined by the phase diagrams of the model with two different strain configurations. In general, we observe that introducing the interaction in the model non-trivially changes the efficiency of the engine for a given pair of bath temperatures as shown in Fig. 7. The efficiency first increases with the interaction, then decreases and increases further. It is observed to be minimal near the regions of phase transitions.

V. CONCLUSIONS

Quantum many-body (MB) systems have been proven to be useful resources for realizing quantum thermal machines (QTMs) as they offer several benefits such as cooperative performance boost, simultaneous achievements of high efficiency and power at the quantum critical points, minimizing frictional effects, and many more. However, the bulk of the existing literature exploring the criticality of MB in the context of QTMs involves models sans the electronic interactions, which are non-trivial to deal with and require sophisticated numerical techniques. At the same time, electronic interactions in conjunction with competing correlations and/or geometric frustration of lattices are known to bring forth rich quantum phases and phase

transitions. To harness quantum criticality for QTM, here we resort to the prototypical Hubbard model in two dimensions (2D) in the framework of the line graph Lieb-kagome lattice as the working medium of a multi-functional QTM. We resort to a non-perturbative, static path approximated (SPA) Monte Carlo technique to deal with the repulsive Hubbard model. We demonstrate that with this model operating between the hot and cold baths one can achieve multiple thermal actions like quantum heat engines, refrigerators, accelerators, and heaters in a quantum Stirling cycle by either engineering the system strain or tuning the bath temperatures.

Furthermore, we show that the heat engine action gets better when the strain is engineered from the kagome limit to the Lieb limit and the refrigeration gets better for the converse. For both cases, in the low-temperature limit, we show that the proposed QTM reaches the ultimate Carnot limit when the temperature difference between the baths is low. The introduction of the onsite Hubbard repulsion allows one to have the Carnot efficiency even in the relatively high-temperature limit while the difference between the two bath temperatures is still close to

zero. It indicates that a relatively higher temperature than the absolute zero is preferred for intermediate interaction strength U while operating a heat engine by engineering the strain from the kagome to the Lieb limit and the converse while operating a refrigerator, near the interaction strength ($U = 4.0t$) for which we get a paramagnetic metal to an anti-ferromagnetic metal, the low-temperature regimes is preferred for both the thermal actions just like the non-interacting case ($U = 0$).

In conclusion, we have modeled a multifunctional QTM, based on a 2D line graph lattice having onsite Hubbard repulsion in the framework of the Lieb and the kagome lattices, which is very efficient. The unprecedented control over the engineering and subsequent tuning of these lattices in ultracold atomic gases, optically induced photonic systems, artificial lattices engineered through lithography and atomic manipulations, and more recently in a metal-organic framework (MOF) make the proposed QTM experimentally realizable in the near future. Therefore, our study can be a stepping stone towards exploring the role of strong electronic interaction, which offers rich phases and phase transitions involving magnetic orders, on QTM.

* madhuparna.k@gmail.com

† avijitmisra0120@gmail.com

- ¹ H. E. D. Scovil and E. O. Schulz-DuBois, “Three-level masers as heat engines,” *Phys. Rev. Lett.* **2**, 262–263 (1959).
- ² R. Alicki, “The quantum open system as a model of the heat engine,” *J. Phys. A* **12**, L103–L107 (1979).
- ³ Victor Mukherjee and Uma Divakaran, “Many-body quantum thermal machines,” *Journal of Physics: Condensed Matter* **33**, 454001 (2021).
- ⁴ Eitan Geva and Ronnie Kosloff, “The quantum heat engine and heat pump: An irreversible thermodynamic analysis of the three level amplifier,” *The Journal of Chemical Physics* **104**, 7681–7699 (1996), <https://doi.org/10.1063/1.471453>.
- ⁵ Loris Maria Cangemi, Chittrak Bhadra, and Amikam Levy, “Quantum engines and refrigerators,” (2023), [arXiv:2302.00726 \[quant-ph\]](https://arxiv.org/abs/2302.00726).
- ⁶ David Gelbwaser-Klimovsky, Wolfgang Niedenzu, and Gershon Kurizki, “Thermodynamics of quantum systems under dynamical control,” *Advances In Atomic, Molecular, and Optical Physics* **64**, 329–407 (2015).
- ⁷ D. Gelbwaser-Klimovsky, R. Alicki, and G. Kurizki, “Minimal universal quantum heat machine,” *Phys. Rev. E* **87**, 012140 (2013).
- ⁸ Tomáš Opatrný, Šimon Bräuer, Abraham G Kofman, Avijit Misra, Nilakantha Meher, Ofer Firstenberg, Eilon Poem, and Gershon Kurizki, “Nonlinear coherent heat machines,” *Science advances* **9**, eadf1070 (2023).
- ⁹ Avijit Misra, Tomáš Opatrný, and Gershon Kurizki, “Work extraction from single-mode thermal noise by measurements: How important is information?” *Physical Review E* **106** (2022), [10.1103/physreve.106.054131](https://doi.org/10.1103/physreve.106.054131).
- ¹⁰ Tomas Opatrny, Avijit Misra, and Gershon Kurizki, “Work generation from thermal noise by quantum phase-sensitive observation,” *Physical Review Letters* **127** (2021), [10.1103/physrevlett.127.040602](https://doi.org/10.1103/physrevlett.127.040602).
- ¹¹ Nathan M Myers, Obinna Abah, and Sebastian Deffner, “Quantum thermodynamic devices: From theoretical proposals to experimental reality,” *AVS quantum science* **4** (2022).
- ¹² Sourav Bhattacharjee and Amit Dutta, “Quantum thermal machines and batteries,” *The European Physical Journal B* **94**, 1–42 (2021).
- ¹³ Tanmoy Pandit, Pritam Chattopadhyay, and Goutam Paul, “Non-commutative space engine: a boost to thermodynamic processes,” *Modern Physics Letters A* **36**, 2150174 (2021).
- ¹⁴ Pritam Chattopadhyay, Tanmoy Pandit, Ayan Mitra, and Goutam Paul, “Quantum cycle in relativistic non-commutative space with generalized uncertainty principle correction,” *Physica A: Statistical Mechanics and its Applications* **584**, 126365 (2021).
- ¹⁵ Debarupa Saha, Aparajita Bhattacharyya, Kornikar Sen, and Ujjwal Sen, “Harnessing energy extracted from heat engines to charge quantum batteries,” (2023), [arXiv:2309.15634 \[quant-ph\]](https://arxiv.org/abs/2309.15634).
- ¹⁶ Saikat Sur and Arnab Ghosh, “Quantum advantage of thermal machines with bose and fermi gases,” *Entropy* **25**, 372 (2023).
- ¹⁷ Gershon Kurizki and Abraham G Kofman, *Thermodynamics and Control of Open Quantum Systems* (Cambridge University Press, 2022).
- ¹⁸ Amikam Levy and Ronnie Kosloff, “Quantum absorption refrigerator,” *Phys. Rev. Lett.* **108**, 070604 (2012).
- ¹⁹ Noah Linden, Sandu Popescu, and Paul Skrzypczyk, “How small can thermal machines be? the smallest possible refrigerator,” *Phys. Rev. Lett.* **105**, 130401 (2010).
- ²⁰ Chiranjib Mukhopadhyay, Avijit Misra, Samyadeb Bhattacharya, and Arun Kumar Pati, “Quantum speed limit constraints on a nanoscale autonomous refrigerator,” *Physical Review E* **97** (2018), [10.1103/physreve.97.062116](https://doi.org/10.1103/physreve.97.062116).
- ²¹ Sreetama Das, Avijit Misra, Amit Kumar Pal, Aditi Sen(De), and Ujjwal Sen, “Necessarily transient quantum refrigerator,” *EPL (Europhysics Letters)* **125**, 20007 (2019).
- ²² Tanaya Ray, Sayan Mondal, Aparajita Bhattacharyya, Ahana Ghoshal, Debraj Rakshit, and Ujjwal Sen, “Kerr-type nonlinear baths enhance cooling in quantum refrigerators,” (2023), [arXiv:2311.10499 \[quant-ph\]](https://arxiv.org/abs/2311.10499).
- ²³ M Tahir Naseem, Avijit Misra, and Özgür E Müstecaplıoğlu, “Two-body quantum absorption refrigerators with optomechanical-like interactions,” *Quantum Science and Technology* **5**, 035006 (2020).
- ²⁴ Cahit Kargı, M. Tahir Naseem, Tomáš Opatrny, Özgür E. Müste-

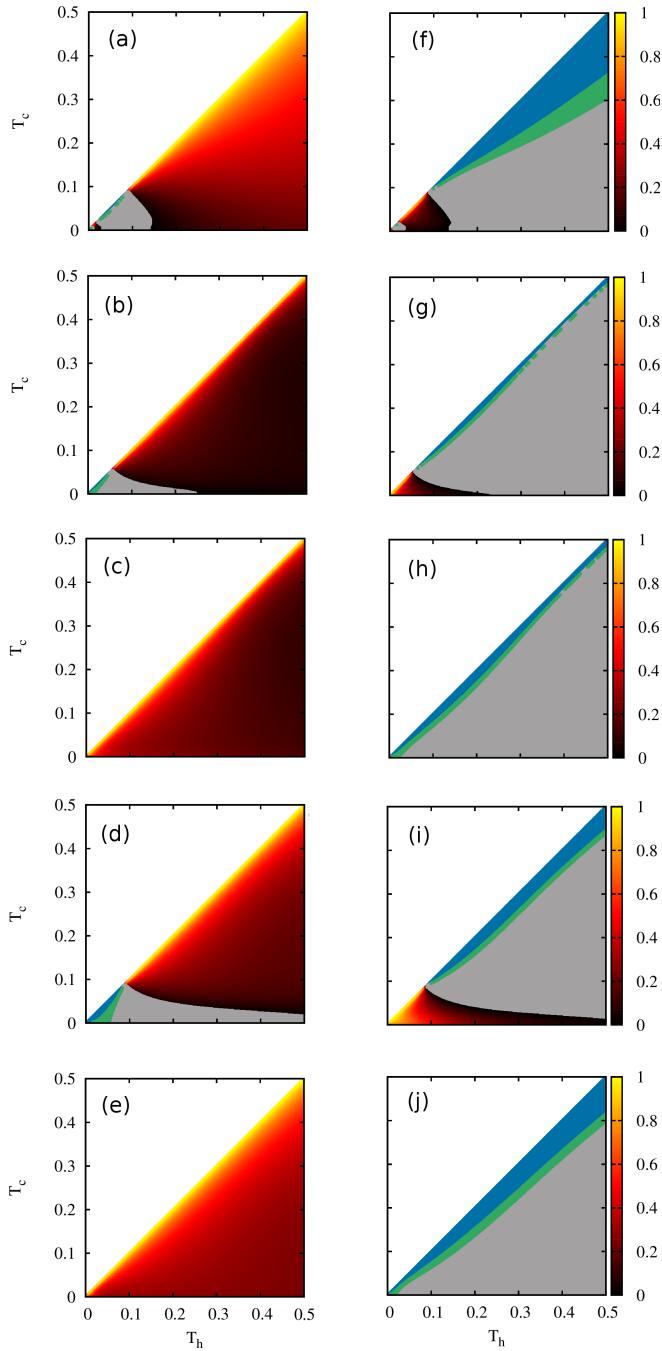


Figure 6. The diagram of modes for a Stirling cycle operating in the refrigerator, the accelerator, and the heater regions are marked in blue, grey, and green respectively. The set of subfigures (a-e) corresponds to the Stirling cycle with strain parameters $(\theta_1 = 2\pi/3, \theta_2 = \pi/2)$ and the set (f-j) correspond to the same with strain parameters $(\theta_1 = \pi/2, \theta_2 = 2\pi/3)$. The Hubbard interaction parameter assumes the following values: $U = 1.0$ in (a) and (f); $U = 3.6$ in (b) and (g); $U = 4.2$ in (c) and (h); $U = 4.6$ in (d) and (i); $U = 9.0$ in (e) and (j). The engine region is plotted with color density where the color denotes the engine efficiency.

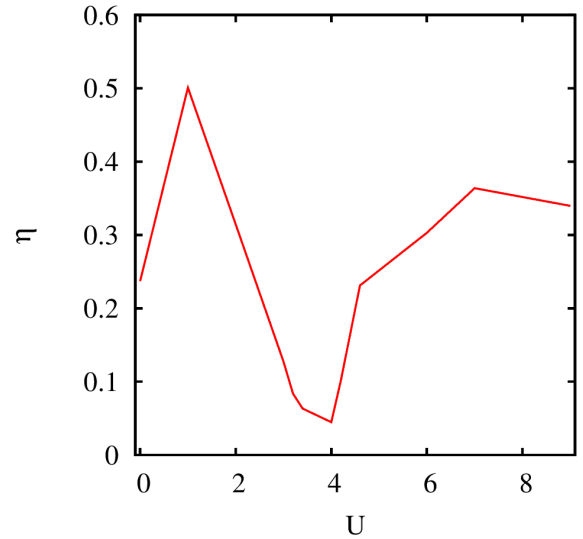


Figure 7. Efficiency ($\theta_1 = 2\pi/3, \theta_2 = \pi/2$) as a function of U for the set of bath temperatures $T_h = 0.5, T_c = 0.3$.

- caphoğlu, and Gershon Kurizki, “Quantum optical two-atom thermal diode,” *Phys. Rev. E* **99**, 042121 (2019).
- ²⁵ Riddhi Ghosh, Ahana Ghoshal, and Ujjwal Sen, “Quantum thermal transistors: Operation characteristics in steady state versus transient regimes,” *Phys. Rev. A* **103**, 052613 (2021).
- ²⁶ Karl Joulain, Jérémie Drevillon, Younès Ezzahri, and Jose Ordóñez-Miranda, “Quantum thermal transistor,” *Physical Review Letters* **116** (2016), 10.1103/physrevlett.116.200601.
- ²⁷ Arghya Maity, Paranjay Chaki, Ahana Ghoshal, and Ujjwal Sen, “Quantum heat transformers,” (2024), [arXiv:2404.00584 \[quant-ph\]](https://arxiv.org/abs/2404.00584).
- ²⁸ Johannes Roßnagel, Samuel T Dawkins, Karl N Tolazzi, Obinna Abah, Eric Lutz, Ferdinand Schmidt-Kaler, and Kilian Singer, “A single-atom heat engine,” *Science* **352**, 325–329 (2016).
- ²⁹ Gleb Maslennikov, Shiqian Ding, Roland Hablützel, Jaren Gan, Alexandre Roulet, Stefan Nimmrichter, Jibo Dai, Valerio Scarani, and Dzmitry Matsukevich, “Quantum absorption refrigerator with trapped ions,” *Nature communications* **10**, 1–8 (2019).
- ³⁰ D. von Lindenfels, O. Gräß, C. T. Schmiegelow, V. Kaushal, J. Schulz, Mark T. Mitchison, John Goold, F. Schmidt-Kaler, and U. G. Poschinger, “Spin heat engine coupled to a harmonic-oscillator flywheel,” *Phys. Rev. Lett.* **123**, 080602 (2019).
- ³¹ John PS Peterson, Tiago B Batalhão, Marcela Herrera, Alexandre M Souza, Roberto S Sarthour, Ivan S Oliveira, and Roberto M Serra, “Experimental characterization of a spin quantum heat engine,” *Physical review letters* **123**, 240601 (2019).
- ³² James Klatzow, Jonas N Becker, Patrick M Ledingham, Christian Weinzetl, Krzysztof T Kaczmarek, Dylan J Saunders, Joshua Nunn, Ian A Walmsley, Raam Uzdin, and Eilon Poem, “Experimental demonstration of quantum effects in the operation of microscopic heat engines,” *Physical Review Letters* **122**, 110601 (2019).
- ³³ Marlan O. Scully, “Extracting work from a single heat bath via vanishing quantum coherence ii: Microscopic model,” *AIP Conf. Proc.* **643**, 83–91 (2002).
- ³⁴ J. Roßnagel, O. Abah, F. Schmidt-Kaler, K. Singer, and E. Lutz, “Nanoscale heat engine beyond the carnot limit,” *Phys. Rev. Lett.* **112**, 030602 (2014).
- ³⁵ Bartłomiej Gardas and Sebastian Deffner, “Thermodynamic uni-

- versality of quantum carnot engines,” *Phys. Rev. E* **92**, 042126 (2015).
- ³⁶ Wolfgang Niedenzu, Victor Mukherjee, Arnab Ghosh, Abraham G. Kofman, and Gershon Kurizki, “Quantum engine efficiency bound beyond the second law of thermodynamics,” *Nature Communications* **9**, 165 (2018).
- ³⁷ Gentaro Watanabe, B Prasanna Venkatesh, Peter Talkner, and Adolfo Del Campo, “Quantum performance of thermal machines over many cycles,” *Physical review letters* **118**, 050601 (2017).
- ³⁸ Patrice A Camati, Jonas FG Santos, and Roberto M Serra, “Coherence effects in the performance of the quantum otto heat engine,” *Physical Review A* **99**, 062103 (2019).
- ³⁹ Cyril Elouard, David A Herrera-Martí, Maxime Clusel, and Alexia Auffèves, “The role of quantum measurement in stochastic thermodynamics,” *npj Quantum Information* **3**, 9 (2017).
- ⁴⁰ Cyril Elouard, David Herrera-Martí, Benjamin Huard, and Alexia Auffèves, “Extracting work from quantum measurement in maxwell’s demon engines,” *Physical Review Letters* **118**, 260603 (2017).
- ⁴¹ Nathanaël Cottet, Sébastien Jezouin, Landry Bretheau, Philippe Campagne-Ibarcq, Quentin Ficheux, Janet Anders, Alexia Auffèves, Rémi Azouit, Pierre Rouchon, and Benjamin Huard, “Observing a quantum maxwell demon at work,” *Proceedings of the National Academy of Sciences* **114**, 7561–7564 (2017).
- ⁴² Jonas FG Santos and Pritam Chattopadhyay, “Pt-symmetry effects in measurement-based quantum thermal machines,” *Physica A: Statistical Mechanics and its Applications* **632**, 129342 (2023).
- ⁴³ Ronnie Kosloff and Yair Rezek, “The quantum harmonic otto cycle,” *Entropy* **19**, 136 (2017).
- ⁴⁴ Juan Jaramillo, Mathieu Beau, and Adolfo del Campo, “Quantum supremacy of many-particle thermal machines,” *New J. Phys.* **18**, 075019 (2016).
- ⁴⁵ Matteo Polettini, Gatién Verley, and Massimiliano Esposito, “Efficiency statistics at all times: Carnot limit at finite power,” *Physical review letters* **114**, 050601 (2015).
- ⁴⁶ Mojde Fadaie, Elif Yunt, and Özgür E. Müstecaplıoğlu, “Topological phase transition in quantum-heat-engine cycles,” *Phys. Rev. E* **98**, 052124 (2018).
- ⁴⁷ Michele Campisi and Rosario Fazio, “The power of a critical heat engine,” *Nat. Commun.* **7**, 11895 (2016).
- ⁴⁸ Nicole Yunger Halpern, Christopher David White, Sarang Gopalakrishnan, and Gil Refael, “Quantum engine based on many-body localization,” *Physical Review B* **99**, 024203 (2019).
- ⁴⁹ Ali Ü C Hardal and Özgür E Müstecaplıoğlu, “Superradiant quantum heat engine,” *Sci. Rep.* **5**, 12953 (2015).
- ⁵⁰ Jiawen Deng, Qing-hai Wang, Zhihao Liu, Peter Hänggi, and Jiangbin Gong, “Boosting work characteristics and overall heat-engine performance via shortcuts to adiabaticity: Quantum and classical systems,” *Phys. Rev. E* **88**, 062122 (2013).
- ⁵¹ A del Campo, John Goold, and Mauro Paternostro, “More bang for your buck: Super-adiabatic quantum engines,” *Scientific reports* **4**, 6208 (2014).
- ⁵² Mathieu Beau, Juan Jaramillo, and Adolfo Del Campo, “Scaling-up quantum heat engines efficiently via shortcuts to adiabaticity,” *Entropy* **18**, 168 (2016).
- ⁵³ Felix Binder, Luis A Correa, Christian Gogolin, Janet Anders, and Gerardo Adesso, “Thermodynamics in the quantum regime,” *Fundamental Theories of Physics* **195**, 1–2 (2018).
- ⁵⁴ J Bengtsson, M Nilsson Tengstrand, A Wacker, P Samuelsson, M Ueda, H Linke, and SM Reimann, “Quantum szilard engine with attractively interacting bosons,” *Physical Review Letters* **120**, 100601 (2018).
- ⁵⁵ Yang-Yang Chen, Gentaro Watanabe, Yi-Cong Yu, Xi-Wen Guan, and Adolfo del Campo, “An interaction-driven many-particle quantum heat engine and its universal behavior,” *npj Quantum Information* **5**, 88 (2019).
- ⁵⁶ Elbio Dagotto, “Complexity in strongly correlated electronic systems,” *Science* **309**, 257 (2005).
- ⁵⁷ Dmytro Pesin and Leon Balents, “Mott physics and band topology in materials with strong spin-orbit interaction,” *Nature Physics* **6**, 376 (2010).
- ⁵⁸ D. N. Basov, Richard D. Averitt, Dirk van der Marel, Martin Dressel, and Kristjan Haule, “Electrodynamics of correlated electron materials,” *Rev. Mod. Phys.* **83**, 471–541 (2011).
- ⁵⁹ Yoshiaki Imai and Norio Kawakami, “Spectral functions in itinerant electron systems with geometrical frustration,” *Phys. Rev. B* **65**, 233103 (2002).
- ⁶⁰ O. Parcollet, G. Biroli, and G. Kotliar, “Cluster dynamical mean field analysis of the mott transition,” *Phys. Rev. Lett.* **92**, 226402 (2004).
- ⁶¹ B. Kyung and A.-M. S. Tremblay, “Mott transition, antiferromagnetism, and *d*-wave superconductivity in two-dimensional organic conductors,” *Phys. Rev. Lett.* **97**, 046402 (2006).
- ⁶² Takuma Ohashi, Tsutomu Momoi, Hirokazu Tsunetsugu, and Norio Kawakami, “Finite temperature mott transition in hubbard model on anisotropic triangular lattice,” *Phys. Rev. Lett.* **100**, 076402 (2008).
- ⁶³ Alexander Wietek, Riccardo Rossi, Fedor Šimkovic, Marcel Klett, Philipp Hansmann, Michel Ferrero, E. Miles Stoudenmire, Thomas Schäfer, and Antoine Georges, “Mott insulating states with competing orders in the triangular lattice hubbard model,” *Phys. Rev. X* **11**, 041013 (2021).
- ⁶⁴ Josef Kaufmann, Klaus Steiner, Richard T. Scalettar, Karsten Held, and Oleg Janson, “How correlations change the magnetic structure factor of the kagome hubbard model,” *Phys. Rev. B* **104**, 165127 (2021).
- ⁶⁵ Andressa R. Medeiros-Silva, Natanael C. Costa, and Thereza Paiva, “Thermodynamic, magnetic, and transport properties of the repulsive hubbard model on the kagome lattice,” *Phys. Rev. B* **107**, 035134 (2023).
- ⁶⁶ Shintaro Taie, Hideki Ozawa, Tomohiro Ichinose, Takuei Nishio, Shuta Nakajima, and Yoshiro Takahashi, “Coherent driving and freezing of bosonic matter wave in an optical lieb lattice,” *Science Advances* **1**, e1500854 (2015).
- ⁶⁷ Hideki Ozawa, Shintaro Taie, Tomohiro Ichinose, and Yoshiro Takahashi, “Interaction-driven shift and distortion of a flat band in an optical lieb lattice,” *Phys. Rev. Lett.* **118**, 175301 (2017).
- ⁶⁸ Rodrigo A. Vicencio, Camilo Cantillano, Luis Morales-Inostroza, Bastián Real, Cristian Mejía-Cortés, Steffen Weimann, Alexander Szameit, and Mario I. Molina, “Observation of localized states in lieb photonic lattices,” *Phys. Rev. Lett.* **114**, 245503 (2015).
- ⁶⁹ Shiqiang Xia, Yi Hu, Daohong Song, Yuanyuan Zong, Liqin Tang, and Zhigang Chen, “Demonstration of flat-band image transmission in optically induced lieb photonic lattices,” *Opt. Lett.* **41**, 1435 (2016).
- ⁷⁰ Seabrata Mukherjee and Robert R. Thomson, “Observation of localized flat-band modes in a quasi-one-dimensional photonic rhombic lattice,” *Opt. Lett.* **40**, 5443 (2015).
- ⁷¹ Robert Drost, Teemu Ojanen, Ari Harju, and Peter Liljeroth, “Topological states in engineered atomic lattices,” *Nature Physics* **13**, 668 (2017).
- ⁷² Marlou R. Slot, Thomas S. Gardenier, Peter H. Jacobse, Guido C. P. van Miert, Sander N. Kempkes, Stephan J. M. Zevenhuizen, Cristiane Morais Smith, Daniel Vanmaekelbergh, and Ingmar Swart, “Experimental realization and characterization of an electronic lieb lattice,” *Nature Physics* **13**, 672 (2017).
- ⁷³ Wen-Xuan Qiu, Shuai Li, Jin-Hua Gao, Yi Zhou, and Fu-Chun Zhang, “Designing an artificial lieb lattice on a metal surface,”

- Phys. Rev. B* **94**, 241409 (2016).
- ⁷⁴ Xiaojuan Ni, Hong Li, Feng Liu, and Jean-Luc Brédas, “Engineering of flat bands and dirac bands in two-dimensional covalent organic frameworks (cofs): relationships among molecular orbital symmetry, lattice symmetry, and electronic-structure characteristics,” *Mater. Horiz.* **9**, 88 (2022).
- ⁷⁵ Shashikant Singh Kunwar and Madhuparna Karmakar, “Kagome hubbard model away from the strong coupling limit: Flat band localization and non fermi liquid signatures,” (2024), [arXiv:2404.05787 \[cond-mat.str-el\]](https://arxiv.org/abs/2404.05787).
- ⁷⁶ George Thomas, Debmalya Das, and Sibasish Ghosh, “Quantum heat engine based on level degeneracy,” *Phys. Rev. E* **100**, 012123 (2019).
- ⁷⁷ S Hamedani Raja, S Maniscalco, G S Paroanu, J P Pekola, and N Lo Gullo, “Finite-time quantum stirling heat engine,” *New Journal of Physics* **23**, 033034 (2021).
- ⁷⁸ Pritam Chattopadhyay and Goutam Paul, “Relativistic quantum heat engine from uncertainty relation standpoint,” *Scientific reports* **9**, 16967 (2019).
- ⁷⁹ Pritam Chattopadhyay, Ayan Mitra, Goutam Paul, and Vasilios Zarikas, “Bound on efficiency of heat engine from uncertainty relation viewpoint,” *Entropy* **23**, 439 (2021).
- ⁸⁰ Pritam Chattopadhyay, “Non-commutative space: boon or bane for quantum engines and refrigerators,” *The European Physical Journal Plus* **135**, 1–11 (2020).
- ⁸¹ J. Hubbard, “Calculation of partition functions,” *Phys. Rev. Lett.* **3**, 77–78 (1959).
- ⁸² H. J. Schulz, “Effective action for strongly correlated fermions from functional integrals,” *Phys. Rev. Lett.* **65**, 2462–2465 (1990).
- ⁸³ Avijit Misra, Uttam Singh, Manabendra Nath Bera, and A. K. Rajagopal, “Quantum rényi relative entropies affirm universality of thermodynamics,” *Physical Review E* **92** (2015), 10.1103/phys-rev.92.042161.
- ⁸⁴ Paul Skrzypczyk, Anthony J. Short, and Sandu Popescu, “Work extraction and thermodynamics for individual quantum systems,” *Nature Communications* **5** (2014), 10.1038/ncomms5185.
- ⁸⁵ Wei Jiang, Meng Kang, Huaqing Huang, Hongxing Xu, Tony Low, and Feng Liu, “Topological band evolution between lieb and kagome lattices,” *Phys. Rev. B* **99**, 125131 (2019).
- ⁸⁶ Wei Jiang, Meng Kang, Huaqing Huang, Hongxing Xu, Tony Low, and Feng Liu, “Topological band evolution between lieb and kagome lattices,” *Physical Review B* **99**, 125131 (2019).
- ⁸⁷ Caitlin Walsh, Maxime Charlebois, Patrick Sémon, Giovanni Sordi, and André-Marie S. Tremblay, *Proceedings of the National Academy of Sciences* **118**, e2104114118 (2021).
- ⁸⁸ C. Walsh, P. Sémon, D. Poulin, G. Sordi, and A.-M. S. Tremblay, “Entanglement and classical correlations at the doping-driven mott transition in the two-dimensional hubbard model,” *PRX Quantum* **1**, 020310 (2020).
- ⁸⁹ C. Walsh, P. Sémon, D. Poulin, G. Sordi, and A.-M. S. Tremblay, “Thermodynamic and information-theoretic description of the mott transition in the two-dimensional hubbard model,” *Phys. Rev. B* **99**, 075122 (2019).
- ⁹⁰ C. Walsh, P. Sémon, D. Poulin, G. Sordi, and A.-M. S. Tremblay, “Local entanglement entropy and mutual information across the mott transition in the two-dimensional hubbard model,” *Phys. Rev. Lett.* **122**, 067203 (2019).
- ⁹¹ Qiong Qin, Jian-Jun Dong, Yutao Sheng, Dongchen Huang, and Yi-feng Yang, “Superconducting fluctuations and charge- $4e$ plaquette state at strong coupling,” *Phys. Rev. B* **108**, 054506 (2023).
- ⁹² R. W. D. Nickalls, “Viète, descartes and the cubic equation,” *The Mathematical Gazette* **90**, 203–208 (2006).

Appendix A: Working Medium: Tight-binding calculation

The electron field operator in the momentum space can be expressed in the quasiparticle basis via Bogoliubov canonical transformation as,

$$c_{i\sigma,k} = \sum_n u_{i\sigma}^n \gamma_{n,k} \quad (\text{A1})$$

$$c_{i\sigma,k}^\dagger = \sum_n u_{i\sigma}^{n*} \gamma_{n,k}^\dagger \quad (\text{A2})$$

where, $\sigma = \pm 1$ corresponds to the spin label and n is the energy index. The operators create (annihilate) a Bogoliubov quasiparticle at state n in the momentum space. The quasiparticle operators satisfy the anti-commutation relations:

$$\{\gamma_{n,k}, \gamma_{m,k}^\dagger\} = \delta_{nm} \quad (\text{A3})$$

$$\{\gamma_{n,k}, \gamma_{m,k}\} = \{\gamma_{n,k}^\dagger, \gamma_{m,k}^\dagger\} = 0 \quad (\text{A4})$$

These relations also guarantee the anti-commutation relations among the original electronic field operators. With the above canonical transformation, the Hamiltonian is diagonalized in the following form:

$$H_k^{\text{diag}} = \sum_n E_n \gamma_{n,k}^\dagger \gamma_{n,k} + E_{\text{const}} \quad (\text{A5})$$

The above Hamiltonian is diagonal in the quasiparticle basis in the momentum space. So, the eigenvalues of the Hamiltonian for a k mode given in Eq. 2 are given by Viéte's formula⁹²,

$$\begin{aligned} \varepsilon_{\mathbf{k},j}^\theta &= \sqrt{\frac{2}{3}} (A_{\mathbf{k}}^2 + B_{\mathbf{k}}^{\theta^2} + C_{\mathbf{k}}^{\theta^2})^{1/2} \times \\ &\cos \left[\frac{1}{3} \cos^{-1} \left(\frac{3\sqrt{3}A_{\mathbf{k}}B_{\mathbf{k}}^\theta C_{\mathbf{k}}^\theta}{(A_{\mathbf{k}}^2 + B_{\mathbf{k}}^{\theta^2} + C_{\mathbf{k}}^{\theta^2})^{3/2}} \right) - \frac{2\pi(j-1)}{3} \right], \\ &j = 1, 2, 3. \end{aligned} \quad (\text{A6})$$

Appendix B: Numerical scheme for interacting Hamiltonian

The repulsive Hubbard Hamiltonian on a 2D line graph Lieb-kagome lattice reads as,

$$\begin{aligned} H &= \mu \sum_{i,\sigma} c_{i,\sigma}^\dagger c_{i,\sigma} + \sum_{\langle ij \rangle, \sigma} t_{ij} c_{i,\sigma}^\dagger c_{j,\sigma} + \text{H. c.} + \sum_{\langle\langle ij \rangle\rangle, \sigma} t'_{ij} c_{i,\sigma}^\dagger c_{j,\sigma} + \text{H. c.} \\ &+ U \sum_i \hat{n}_{i\uparrow} \hat{n}_{i\downarrow}. \end{aligned} \quad (\text{B1})$$

where, t_{ij} corresponds to the nearest neighbor hopping and $t_{ij} = t = 1$ sets the reference energy scale of the model. The applied strain is quantified in terms of $t'_{ij} = t'$. $U > 0$ corresponds to the repulsive Hubbard interaction. We work at the half-filling and the chemical potential μ is adjusted to achieve the same. In order to make the model numerically tractable we decompose the interaction term using Hubbard Stratonovich (HS) decomposition and thereby introduce two (bosonic) auxiliary fields viz. a vector field $\mathbf{m}_i(\tau)$ and a scalar field $\phi_i(\tau)$, which couples to the spin and charge densities, respectively. The introduction of these auxiliary fields aids in capturing the Hartree-Fock theory at the saddle point and retains the spin rotation invariance and the Goldstone modes.

In terms of the Grassmann fields $\psi_{i\sigma}(\tau)$, we have,

$$\exp \left[U \sum_i \bar{\psi}_{i\uparrow} \psi_{i\uparrow} \bar{\psi}_{i\downarrow} \psi_{i\downarrow} \right] = \int \prod_i d\phi_i d\mathbf{m}_i \exp \left[\frac{\phi_i^2}{U} + i\phi_i \rho_i + \frac{m_i^2}{U} - 2\mathbf{m}_i \cdot \mathbf{s}_i \right] \quad (\text{B2})$$

where, the charge and spin densities are defined as, $\rho_i = \sum_\sigma \bar{\psi}_{i\sigma} \psi_{i\sigma}$ and $\mathbf{s}_i = (1/2) \sum_{a,b} \bar{\psi}_{ia} \sigma_{ab} \psi_{ib}$, respectively. The

corresponding partition function thus takes the form,

$$\mathcal{Z} = \int \prod_i \frac{d\bar{\psi}_{i\sigma} d\psi_{i\sigma} d\phi_i d\mathbf{m}_i}{4\pi^2 U} \exp \left[- \int_0^\beta \mathcal{L}(\tau) \right] \quad (\text{B3})$$

where, the Lagrangian \mathcal{L} is defined as,

$$\mathcal{L}(\tau) = \sum_{i\sigma} \bar{\psi}_{i\sigma}(\tau) \partial_\tau \psi_{i\sigma}(\tau) + H_0(\tau) + \sum_i \left[\frac{\phi_i(\tau)^2}{U} + (i\phi_i(\tau) - \mu)\rho_i(\tau) + \frac{m_i(\tau)^2}{U} - 2\mathbf{m}_i(\tau) \cdot \mathbf{s}_i(\tau) \right] \quad (\text{B4})$$

where, H_0 is the kinetic energy contribution. The ψ integral is now quadratic but at the cost of an additional integration over the fields $\mathbf{m}_i(\tau)$ and $\phi_i(\tau)$. The weight factor for the \mathbf{m}_i and ϕ_i configurations can be determined by integrating out the ψ and $\bar{\psi}$, and using these weighted configurations one goes back and computes the fermionic properties. Formally,

$$\mathcal{Z} = \int \mathcal{D}\mathbf{m} \mathcal{D}\phi e^{-S_{eff}\{\mathbf{m}, \phi\}} \quad (\text{B5})$$

$$S_{eff} = \log \text{Det}[\mathcal{G}^{-1}\{\mathbf{m}, \phi\}] + \frac{\phi_i^2}{U} + \frac{m_i^2}{U} \quad (\text{B6})$$

where, \mathcal{G} is the electron Green's function in a $\{\mathbf{m}_i, \phi_i\}$ background.

The weight factor for an arbitrary space-time configuration $\{\mathbf{m}_i(\tau), \phi_i(\tau)\}$ involves computation of the fermionic determinant in that background. The auxiliary field quantum Monte Carlo with static path approximation (SPA) retains the full spatial dependence in \mathbf{m}_i and ϕ_i but keeps only the $\Omega_n = 0$ mode. It thus includes classical fluctuations of arbitrary magnitudes but no quantum ($\Omega_n \neq 0$) fluctuations. The resulting model can be thought of as fermions coupled to the spatially fluctuating random background of the classical field \mathbf{m}_i . With these approximations, the effective Hamiltonian corresponds to a coupled spin-fermion model, which reads as

$$\begin{aligned} H_{eff} = & \sum_{\langle ij \rangle, \sigma} t_{ij} [c_{i\sigma}^\dagger c_{j\sigma} + h.c.] + \sum_{\langle\langle ij \rangle\rangle, \sigma} t'_{ij} [c_{i\sigma}^\dagger c_{j\sigma} + h.c.] + \sum_{i\sigma} \left(\frac{U}{2} - \mu \right) \hat{n}_{i\sigma} \\ & - \frac{U}{2} \sum_i \mathbf{m}_i \cdot \boldsymbol{\sigma}_i + \frac{U}{4} \sum_i m_i^2 \end{aligned} \quad (\text{B7})$$

where the last term corresponds to the stiffness cost associated with the now classical field \mathbf{m}_i and $\sigma_i = \sum_{a,b} c_{ia}^\dagger \sigma_{ab} c_{ib} = \mathbf{s}_i$.

The random background configurations of $\{\mathbf{m}_i\}$ are generated numerically via Monte Carlo simulation and obey the Boltzmann distribution,

$$P\{\mathbf{m}_i\} \propto \text{Tr}_{c,c^\dagger} e^{-\beta H_{eff}} \quad (\text{B8})$$

For large and random configurations the trace is computed numerically, wherein we diagonalize H_{eff} for each attempted update of \mathbf{m}_i and converge to the equilibrium configuration using Metropolis algorithm. Evidently, the process is numerically expensive and involves an $\mathcal{O}(N^3)$ computational cost per update (where $N = 3 \times L \times L$ corresponds to the system size), thus the cost per MC sweep is N^4 . We cut down on the computation by using the traveling cluster algorithm, wherein instead of diagonalizing the entire lattice for each attempted update of \mathbf{m}_i we diagonalize a smaller cluster surrounding the update site. The computation cost now scales as $\mathcal{O}(NN_c^3)$ (where N_c is the size of a smaller cluster surrounding the update site), which is linear in lattice size N . This allows us to access large system sizes, which is essential to capture the inhomogeneity of the underlying magnetic phase.